Croatian Society for Materials Protection

Metalurgija/Metallurgy

Vol. 65 No. 3 / 2026

Research on Metallurgical Properties and Dynamics of Lump Ore Reduction under Ammonia Conditions

Lanjie Li [1,*], Xing Han [2], Heng Ji [1], Renguo Li [1], Yuejun Liu [3], and Xianchun Li [3,*]

https://doi.org/10.64486/m.65.3.9

[1] HBIS Material Technology Research Institute, Shijiazhuang 050023, Hebei, China
[2] The Strategy Research Institute, HBIS Group Co., Ltd., Shijiazhuang 050023, Hebei, China
huanr4585@163.com
[3] School of Chemical Engineering, University of Science and Technology Liaoning, Anshan 114051 China
* Correspondence: lilanjie@hbisco.com; Tel.: 15003240721, askd1972@163.com; Tel.: 15141212188

Type of the Paper: Article
Received: September 19, 2025
Accepted: January 9, 2026

Abstract: Employing ammonia (NH_3) as a reducing agent for iron ore has become an emerging research direction. High-temperature thermogravimetric analysis equipment was used to study the reduction degree and isothermal kinetics of NH_3-reduced lump ore (L1) within the temperature range of 800 °C–950 °C. Meanwhile, the low-temperature reduction disintegration performance of L1 at 500 °C was investigated. Under conditions of 900 °C and a 60 % NH_3 concentration, a metallization rate of 98.26 % was achieved. The reduction process produced nitric oxide (NO) concentrations as high as 431 ppm. As the reaction progresses, the NO concentration gradually decreases. At 500 °C, as the concentration of NH_3 increased, the specific surface area, pore size, and reduction disintegration degree of the reduced sample all increased. Kinetic analysis shows that the diffusion and geometric shrinkage models can well describe the reduction process of lump ores. The activation energy values derived from both model-fitting and model-free approaches for L1 reduction using 60 % NH_3 were determined to be 64.78 kJ/mol and 61.60 kJ/mol, respectively.

Keywords: ammonia; lump ores; hydrogen; metallurgical properties; kinetics

1. Introduction

The traditional blast furnace ironmaking process has caused serious environmental pollution problems due to the consumption of large amounts of coke [1]. To promote energy efficiency and minimize environmental impact, implementing H_2 as a reductant in vertical furnaces to directly reduce iron ore is an effective approach [2], [3]. Compared with commonly used iron ore pellets in shaft furnaces, lump ores have the advantages of no need for high-temperature block making, high porosity, and a wide source [4]. Therefore, appropriately increasing the proportion of lump ores in the raw materials can further reduce carbon emissions and ironmaking costs [5].

Recently, research on the metallurgical properties and reduction behavior of lump ores has received considerable attention [6], [7]. Generally speaking, the higher the content of goethite (FeOOH) in lump ores, the higher the content of newly generated porous hematite after heating, indicating that the lump ores have excellent reducibility [8]. However, the inherent crystalline water content in lump ores can induce thermal fracturing during the heating process, potentially leading to poor low-temperature reduction disintegration performance,

which may adversely affect the gas permeability and operational efficiency in shaft furnace operations [9]. The reduction disintegration phenomenon of iron ores mainly occurs in the temperature range of 450 °C to 650 °C in the shaft furnace [10]. The developed internal pore structure in lump ores promotes the release of steam pressure within the particles, leading to thermal cracking during the reduction process and the formation of surface cracks in goethite. A composition containing 60 % lump ores in the raw material mixture may initiate substantial degradation in the low-temperature disintegration characteristics of the furnace burden [11]. Research has shown that high-temperature pretreatment of lump ores can transform the ore's internal configuration from a compact state to a plate-like structure, thereby improving its reactivity [12], [13]. In addition, the reduction disintegration characteristics of ores in a hydrogen-rich atmosphere are influenced by the reaction of hematite to magnesite [14], carbon deposition reactions [15], and gangue impurities [16], [17]. To reduce the disintegration degree of lump ore, the proportion of H_2 in the reducing gas can be increased and rapidly reduced at higher temperatures [18]. It is necessary to determine whether the metallurgical properties of the lump ores meet the standards of a vertical furnace.

However, H_2 has the disadvantages of high liquefaction temperature [19], flammability and explosiveness [20], and high storage and transportation costs [21]. Under the current technological conditions, it is difficult to widely promote the application of pure H_2-based metallurgy. NH_3 serves as an efficient hydrogen transport medium, offering significant benefits in the lower liquefaction costs [22], [23] and mature supply processes [24]. At present, NH_3-based metallurgy has become a highly promising clean ironmaking process [25–27]. Iwamoto et al. [28] demonstrated that the NH_3 utilization rate of lump ores is higher after high-temperature pretreatment. Notably, FeOOH exhibits catalytic activity toward NH_3 decomposition [29], [30]. However, there is currently no further research on the application of NH_3 for lump ore reduction. On the other hand, a comprehensive investigation into the reduction kinetics of lump ores is essential to meet the needs of NH_3 metallurgical reaction process development and reactor design. Therefore, to promote cost reduction and efficiency improvement in the steel production processes, investigating the metallurgical properties and reduction kinetics of NH_3 reduced lump ores represents valuable research.

This study systematically examines the influence of NH_3 concentration and reduction temperature on the low-temperature reduction disintegration index (RDI) and reduction degree (α) of NH_3-reduced lump ores. The exhaust gas was measured by a mass spectrometer and an infrared analyzer. Furthermore, the kinetics of NH_3 reduction of lump ores were studied, providing a fundamental basis for optimizing shaft furnace operations in NH_3-based metallurgy in shaft furnaces.

2. Materials and experimental

2.1. Materials

The purities of NH_3 and Argon (Ar) used in the experiment are 99.999 % and 99.99 % respectively. The lump ore (L1) used in this study was provided by HBIS Group Co., Ltd (HBIS) Material Technology Research Institute. To compare the reduction degree of lump ore and iron ore pellets under ammonia conditions [31], the lump ore was crushed and samples with particle sizes of 8 mm–12.5 mm were screened out before the experiment. As Table 1 reveals, the total iron grade (TFe), silicon dioxide (SiO_2), wüstite (FeO), and calcium oxide (CaO) content in L1 are 62.55 %, 1.22 %, 0.03 %, and 0.36 %, respectively. The phase composition of L1 was investigated using X-ray diffraction (XRD) technology, as shown in Figure 1(a). The characteristic diffraction peaks of Fe_2O_3 (JCPDS 33-0664) [32] were detected at 2θ = 24.2°, 35.6°, 49.5°, 57.6°, 62.4°, 72.0°, 75.2°, 77.8°, and 88.6°, whereas distinct diffraction patterns corresponding to FeOOH [33] (JCPDS 81-0462) were observed at 2θ = 17.8°, 21.2°, 26.3°, 33.2°, 34.7°, 36.7°, 40.0°, 41.2°, 47.3°, 50.6°, 53.2°, 54.2°, 59.1°, 61.5°, 63.9°, 65.6°, 67.1°, 67.9°, 69.0°, 69.2°, 71.5°, 79.9°. 81.4°, 84.0°, and 86.3°. Besides, the characteristic diffraction peaks corresponding to SiO_2 [34] (JCPDS 29-0085) were detected at 2θ = 39.5°, 42.5°, 45.8°, 50.1°, 54.9°, 60.0°, and 85.0°. Therefore, L1 is mainly composed of goethite and hematite, and the impurities are mainly quartz.

https://doi.org/10.64486/m.65.3.9

Figures 1(b) to 1(c) show the results of scanning electron microscopy and energy dispersive X-ray spectroscopy (SEM-EDS) analysis of L1. Goethite and hematite were closely intertwined, with Figures 1(b) to 1(c) showing the results of scanning electron microscopy and energy dispersive X-ray spectroscopy (SEM-EDS) analysis of L1. Goethite and hematite were closely intertwined, with the pores in the raw ore were small and evenly distributed. Iron (Fe) and oxygen (O) elements were uniformly distributed in L1. In contrast, the content of silicon (Si), magnesium (Mg), and calcium (Ca) elements was relatively low (in Figure 1 (c)).

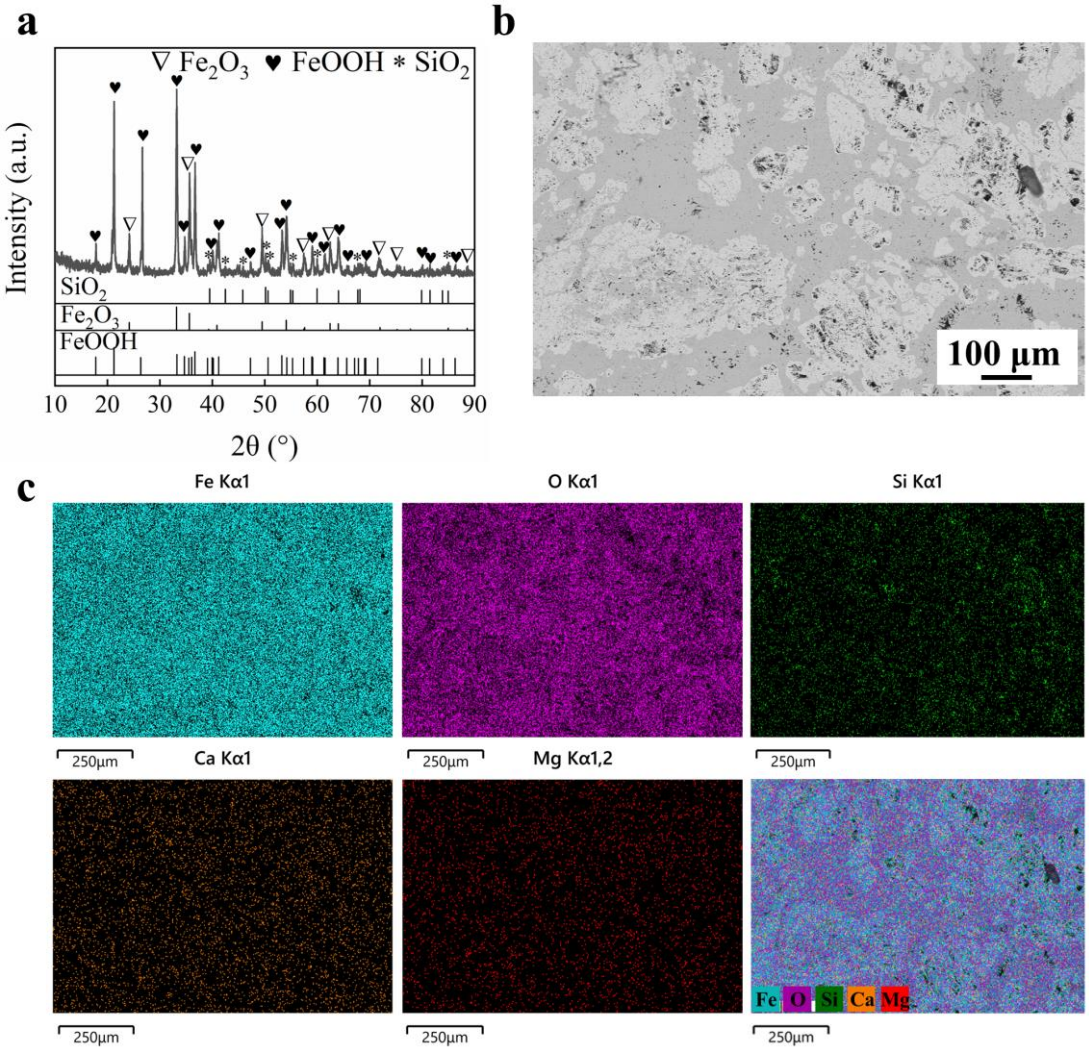

Figure 1. (a) XRD pattern, (b) SEM analysis and (c) EDS mapping results of L1.

Table 1. Chemical composition analysis of L1 (all in ωt.%).

TFe	FeO	SiO_2	Al_2O_3	MgO	P	S	CaO	TiO_2	Mn	LOI1000
62.55	0.36	1.22	0.64	0.06	0.08	0	0.03	0.02	0.04	8.36

2.2. Reactor system and reduction procedure

Based on the GB/T 24189-2024 (equivalent to ISO 7215:2015) standard, the experimental steps for determining the reducibility of lump ores are as follows: A 510 g L1 sample was subjected to drying in an oven at 105 °C for a duration of 120 minutes to achieve a stable weight. For preheating, the reactor's base was layered with Al_2O_3 spheres measuring 8 mm in diameter. A (500 ± 0.5) g L1 sample was loaded over the Al_2O_3 ball, the reactor

https://doi.org/10.64486/m.65.3.9

was sealed and placed in the center of the furnace. To measure the side wall temperature and reactor center temperature separately, place a thermocouple on each furnace side wall and reactor center. A balance was placed above the reactor, and the reactor was hung on the hook of the balance by a lifting rope. The balance can be used to detect the sample quality of iron ore and the reactor in real-time. To eliminate the influence of the carrier gas on the reaction, Ar was chosen as the carrier gas. Before the reaction began, Ar was introduced to blow the reactor to eliminate excess air. To compare the effect of temperature on the reduction degree, we set the reduction temperature as 800 °C, 850 °C, 900 °C and 950 °C. Increase the furnace temperature to the target values at a heating rate of 6 °C/min. After the furnace temperature stabilized, different concentrations of NH_3 (40 %, 50 %, and 60 %) were configured through a mass flow meter and introduced into the reactor. To minimize the impact of flow rate on reduction degree and reduction temperature, and we set the total gas flow rate as 7.5 L/min. According to GB/T 24189-2024 standard, after the reaction time reached 180 minutes, stop the supply of reducing gas and cool the furnace charge in an Ar atmosphere. The experimental reaction system is shown in Figure 2.

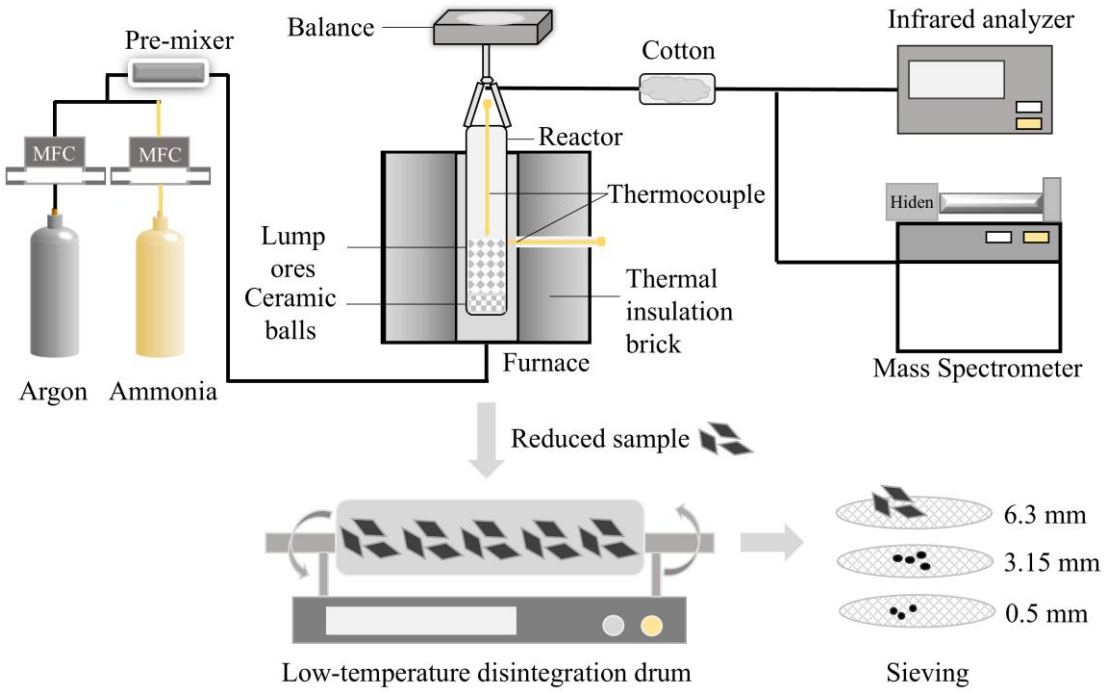

Figure 2. Schematic diagram of experimental setup and process.

Based on the GB/T 13242-2017 standard, the experimental apparatus for determining the RDI of lump ore was the same as that for determining the reducibility. Take (500 ± 0.5) g of the L1 sample after drying, and introduce it into the reactor. The furnace was heated to 500 °C at a heating rate of 6 °C/min while maintaining an Argon atmosphere for protection. After the furnace temperature stabilized, different concentrations of NH_3 (20 %, 40 %, and 60 %) were introduced into the reactor for 60 minutes of reduction at a total flow rate of 7.5 L/min. After the reaction was complete, the reduced sample was allowed to cool down to ambient temperature under an Ar environment. Put the cooled sample into a rotary drum and rotate it at a speed of 30 r/min for 300 r, then use a hole with a width of 6.30 mm, 3.15 mm, and 0.5 mm square hole sieves. Record the sample quality left on each sieve.

After the outlet gas was dried by cotton, the air flow was divided into three paths after passing through the three-way pipe. One of the gases was sent to an infrared analyzer (IR analyzer, China Maihak QGS-08CN) after drying for real-time monitoring of NH_3 and NO concentrations. The IR analyzer needed to be preheated for 2 h, and the working temperature was about 46 °C. Meanwhile, the other stream was channeled to a mass

https://doi.org/10.64486/m.65.3.9

spectrometry analyzer (MS, England HPR-20 R&D) for measuring the concentrations of H_2 and N_2. The tail gas enters the mass spectrometer after being heated by an inert quartz capillary at 120 ℃, and the injection flow was 20 mL/min. The external standard method was employed to calibrate the MS.

2.3. Analytical methods and Characterization

The α value for L1 was determined based on the weight loss of the sample, using the following formula:

$$\boldsymbol{\alpha = (m_1 - m_2)/m_0 \times (0.430\omega_2 - 0.111\omega_1) \times 10^2} \quad (1)$$

Where $\boldsymbol{m_0}$, $\boldsymbol{m_1}$, and $\boldsymbol{m_2}$ correspond to the initial weight of the sample, the mass weight after heating, and the sample weight after reduction (g), respectively. Additionally, ω_1 and ω_2 represent the mass fraction of FeO and TFe, (%), respectively.

The low-temperature RDI is analyzed using the equations given in (2)–(4).

$$\mathbf{RDI}_{+6.3\ mm} = \frac{\boldsymbol{m_{D1}}}{\boldsymbol{m_{D0}}} \times \mathbf{100} \quad (2)$$

$$\mathbf{RDI}_{+3.15\ mm} = \frac{\boldsymbol{m_{D1} + m_{D2}}}{\boldsymbol{m_{D0}}} \times \mathbf{100} \quad (3)$$

$$\mathbf{RDI}_{-0.5\ mm} = \frac{\boldsymbol{m_{D0} - (m_{D1} + m_{D2} + m_{D3})}}{\boldsymbol{m_{D0}}} \times \mathbf{100} \quad (4)$$

In the above formula, m_{D0}, m_{D1}, m_{D2}, and m_{D3} represent the sample mass before the reduction drum, the sample mass remaining on the 6.30 mm sieve, the sample mass remaining on the 3.15 mm sieve, and the mass remaining on the 0.5 mm sieve, respectively. The evaluation of experimental results is based on the results of $RDI_{+3.15\ mm}$ as the assessment indicators, while $RDI_{+6.3\ mm}$ and $RDI_{-0.5\ mm}$ are only used as reference indicators.

The metallization rate (η) is expressed as follows:

$$\boldsymbol{\eta = \mathrm{MFe}/\mathrm{TFe}} \quad (5)$$

Where MFe represents the mass fraction of metallic Fe (%).

Table 2. Summary of commonly used gas-solid reaction models [35]

Model	Symbol	Mechanism	G (α)
Nucleation and nucleus growth models	N1	A-E	$[-\ln(1-\alpha)]^{2/3}$
	N2	A-E	$[-\ln(1-\alpha)]^{1/2}$
Diffusion model	D1	1-D diffusion	α^2
	D2	D diffusion	$\alpha+(1-\alpha)\cdot\ln(1-\alpha)$
Reaction-order models	F1	Zero-order	α
	F2	First-order	$-\ln(1-\alpha)$
	F3	Three-halves order	$2((1-\alpha)^{-1/2}-1)$
	F4	Second-order	$(1-\alpha)^{-1}-1$
Geometrical contraction models	R1	Contracting cylinder	$1-(1-\alpha)^{1/2}$
	R2	Contracting sphere	$1-(1-\alpha)^{1/3}$

https://doi.org/10.64486/m.65.3.9

The kinetic parameters of L1 were determined using both the model-fitting and model-free approaches. The reaction rates $d\alpha/dt$ are described by equations (6)–(7):

$$d\alpha/dt = Aexp^{-Ea/RT} \times f(\alpha) \quad (6)$$

$$G(\alpha) = \int_0^t d\alpha/f(\alpha) = k(T) \times t \quad (7)$$

Where A and k(T) refer to the preexponential factor and the reaction rate constant, 1/s, respectively. Ea is the activation energy, kJ/mol. R is the standard molar gas constant, J/(mol·K). t represents time, s. T refers to the reduction temperature, K. f(α) and G(α) represent the typical gas-solid reaction equations and their corresponding integral expressions that describe the reaction mechanism, respectively. Table 2 provides a summary of the integral forms for gas-solid reaction models [36].

The samples are labeled as L1-aaa-bbNH_3, where xxx denotes the reduction temperature (aaa = 500 °C, 800 °C, 850 °C, 900 °C, and 950 °C). bb represents the initial NH_3 concentration (x = 20 %, 40 %, 50 %, and 60 %).

The phase composition of the samples, both before and after reduction, was analyzed using XRD (Germany, Bruker D8). The analysis was conducted within a range of 10° to 90°. The X-ray source utilized a Cu target, emitting characteristic Kα radiation with a wavelength of 0.154 nm, and operated at a tube voltage of 40 kV. Both pre- and post-reduction samples were encapsulated in epoxy resin for examination. The sample was ground, polished, and mounted using metallographic equipment (China, Kejing Unipol-1200M). The cross-sectional mineral facies of the sample were examined using OM (Germany, ZEISS Axioskop A1). Additionally, the mineral phase structure was analyzed using SEM (Zeiss GeminiSEM 300, Germany) in backscattered electron imaging (BSE) mode. Meanwhile, EDS technology (Oxford Xplorer30, UK) was employed to analyze the cross-sectional element distribution and quantify elemental composition of the sample. The acceleration voltage was 3 kV when photographing the morphology, 15 kV when photographing the energy spectrum mapping, and the detector was SE2 secondary electron detector. The specific surface area and pore size distribution, both before and after reduction, were measured using a specific surface area analyzer (America, Quantachrome Nova3000e). The sample was degassed in vacuum at 150 °C for 8 h.

3. Results and Discussion

3.1. Reduction Behavior

Figure 3 displays the α curves of the reduced samples during the reduction of L1 by NH_3 at different concentrations, the minimum temperature of the reactor's center ($T_{center, min}$), and the XRD results of the reduced samples. As Figure 3(a) shows, when the reduction temperatures were 950 ℃, 900 ℃, 850 ℃, and 800 ℃, and the reduction reaction lasted for 30 minutes, the α values of the samples were 0.59, 0.51, 0.41, and 0.37, respectively. At this temperature condition, when the reaction proceeded for 90 minutes, the α values of L1 were 0.96, 0.92, 0.82, and 0.80, respectively. Meanwhile, after 180 min of reaction, the α values of the samples were 1, 1, 0.98, and 0.96, respectively. Therefore, it can be concluded that in the initial reduction stage, raising the reduction temperature can greatly improve the reduction rate. However, as the reduction time further increased, the rate of the reduction reaction decreased significantly. This is because the reaction from FeO to Fe requires a higher reduction potential [37]. The same phenomenon was also confirmed at NH_3 concentrations of 50 % and 40 % (in Figure 3(b) and Figure 3(c)). As Figure 3(d) indicates, under the conditions of NH_3 concentration of 50 % and 60 % and temperature range of 800 ℃–950 ℃, only the characteristic diffraction peaks of Fe (JCPDS 06-0696) were observed in the reduced sample at 2θ = 44.7°, 65.0°, and 82.3°, suggesting that the reduction of L1 is nearly complete under these conditions. However, under the conditions of an NH_3 concentration of 40 % and a temperature of 800 ℃, alongside the Fe characteristic diffraction peaks, the FeO characteristic diffraction peaks (JCPDS 06-0615) [38] were also detected at 2θ = 36.2°, 42.0°, 51.5°, 60.9°, and 72.9° in the reduced sample, indicating insufficient reduction under these conditions. The gangue in the sample after NH_3 reduction of L1 was

https://doi.org/10.64486/m.65.3.9

mainly composed of SiO_2. In addition, during the reduction of L1 by NH_3, the value of $T_{center, min}$ was lower than the actual preset reduction temperature, indicating that the process is an endothermic reaction (in Figures 3(g) to 3(i)). This conclusion is consistent with previous research [37], [39]. When the temperature was constant, the value of $T_{center, min}$ gradually decreased as the NH_3 concentration rose, suggesting that the heat absorption increases with the increase of NH_3. As Table 3 shows, the FeO content of the reduced samples under the temperature conditions of 950 °C, 900 °C, 850 °C, and 800 °C was 0.75 %, 1.22 %, 4.53 %, and 6.06 %, respectively. This indicates that there is still partially oxidized FeO at temperatures of 800 °C and 850 °C. Owing to the minimal FeO content in its sample, it was not detected by XRD technology. In addition, the samples reduced at 800 °C and 850 °C also had higher levels of SiO_2, aligning with the SEM results. As the temperature decreased, the metallization rate also declined. At an NH_3 concentration of 60 %, the metallization rate can achieve a maximum of 98.94 %.

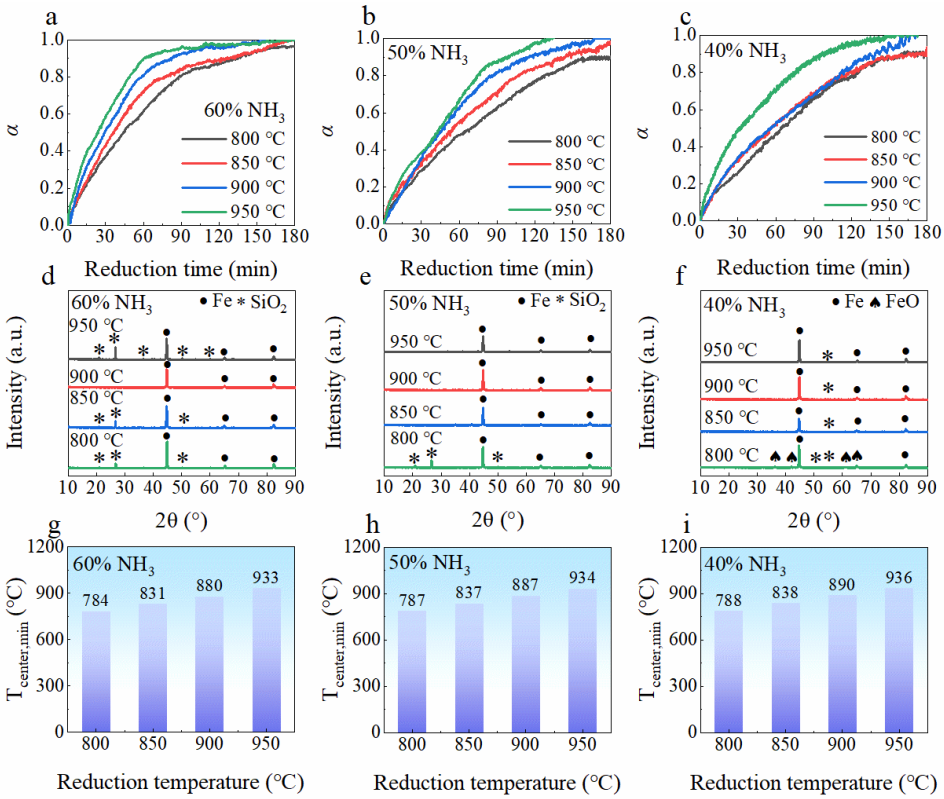

Figure 3. The α curves during the reduction of L1 under various NH_3 concentrations: (a) 60 % NH_3, (b) 50 % NH_3 and (c) 40 % NH_3. XRD pattern of the reduced sample by (d) 60 % NH_3, (e) 50 % NH_3, and (f) 40 % NH_3. The variation of the $T_{center, min}$ under different conditions: (g) 60 % NH_3, (h) 50 % NH_3, and (i) 40 % NH_3.

Table 3. The metallization rate of the sample after 60 % NH_3 reduction of L1

Reduced sample	η/%	TFe/%	MFe/%	FeO/%	SiO_2/%
L1-950 °C-60 % NH_3	98.94	97.56	96.63	0.75	0.81
L1-900 °C-60 % NH_3	98.26	97.08	95.39	1.22	1.18
L1-850 °C-60 % NH_3	96.89	90.82	88.00	4.53	12.07
L1-800 °C-60 % NH_3	94.58	86.87	82.16	6.06	10.20

https://doi.org/10.64486/m.65.3.9

Figure 4 depicts the SEM-EDS analysis results of the samples after reduction at various temperatures. As Figure 4(a) indicates, a large amount of quartz was distributed in the sample of L1-800 °C-60 % NH_3. The area at point 1 was dominated by Fe, with very little O content, suggesting that the white mineral phase is likely metallic Fe. Point 2 was mainly composed of Fe, Si, and O, suggesting that the dark gray mineral phase corresponded to a mixture of FeO and SiO_2. Moreover, Point 3 primarily consisted of Fe, Si, and O, suggesting that the mineral phase structure was composed of a mixture of Fe and SiO_2. In contrast, at a temperature of 950 °C, Points 4, 5, and 6 were primarily composed of Fe with minor amounts of Si and O. The distribution of metallic Fe in the reduced sample was more concentrated, and the sintering phenomenon was more obvious (in Figure 4(b)).

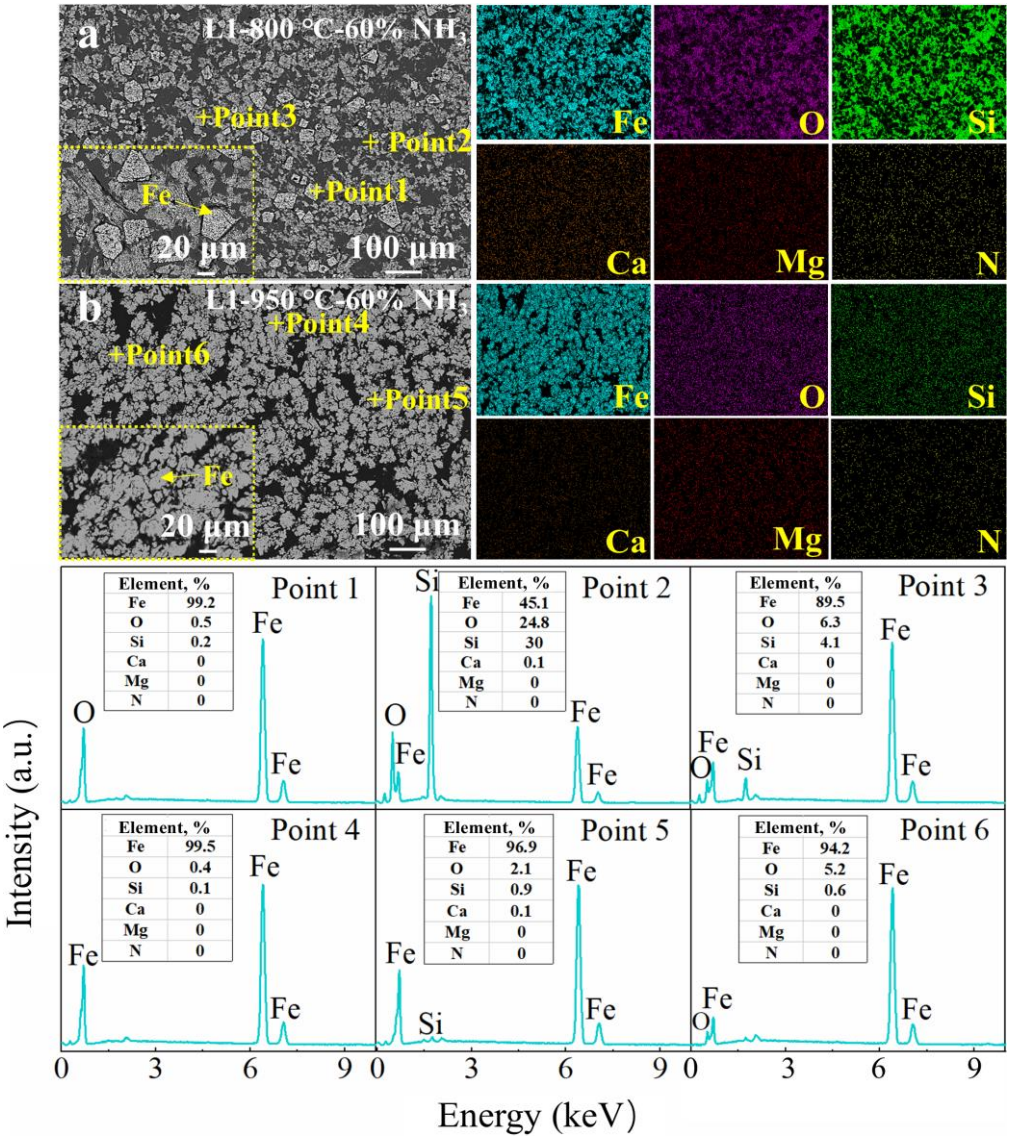

Figure 4. SEM-EDS analysis of the reduced samples: (a) L1-800 °C-60 % NH_3, and (b) L1-950 °C-60 % NH_3.

As Figure 5 demonstrates, at temperatures of 900 °C and 950 °C, the sample reduced by 60 % NH_3 exhibited significant amounts of metallic Fe with a white appearance. Meanwhile, there was still a small amount of FeO in the reduced sample. When the temperature dropped to 850 °C, the agglomeration phenomenon of Fe significantly weakened. However, obvious cracks appeared in the sample of L1-800 °C-60 % NH_3, and the mineral

https://doi.org/10.64486/m.65.3.9

phase presented different structures. This can be explained as the decomposition of crystal water in goethite during the heating process, resulting in a significant increase in the size of sample particles and subsequent shrinkage [40], which leads to the formation of surface cracks on the sample.

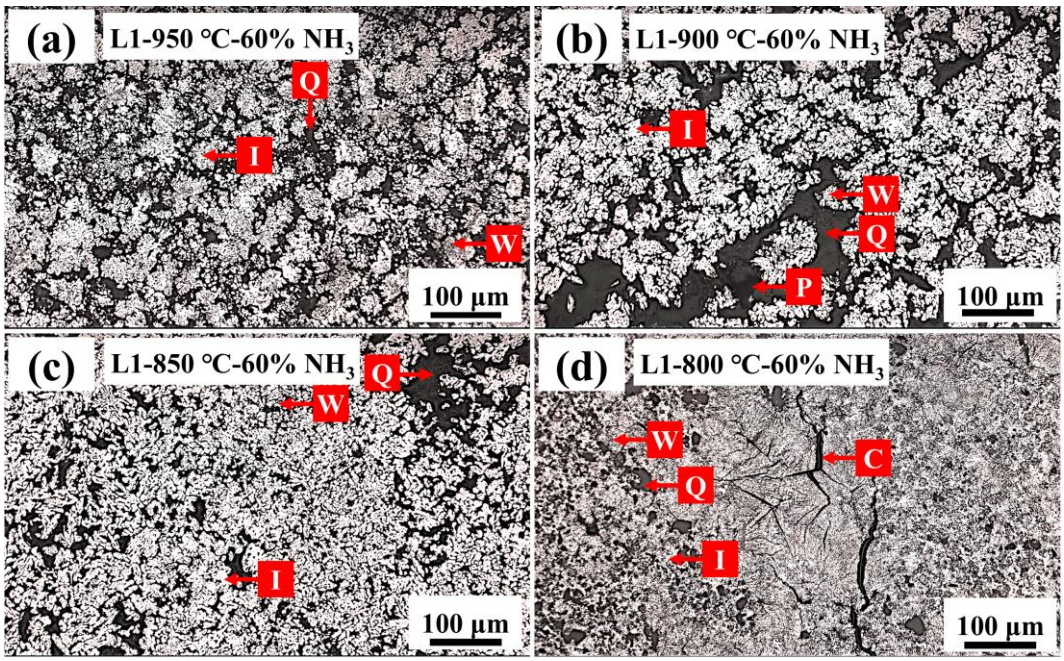

Figure 5. OM analysis of the reduced samples under different temperatures: (a) L1-950 °C-60 % NH_3, (b) L1-900 °C-60 % NH_3, (c) L1-850 °C-60 % NH_3, and (d) L1-800 °C-60 % NH_3. (P: pore. Q: quartz. C: crack. I: Fe. W: wüstite.)

Figures 6 illustrate the changes in TG and gas concentration at the reactor outlet during the reduction of L1 by NH_3 under different conditions. According to theoretical calculations, if 60 % of NH_3 is completely decomposed, approximately 57 % of H_2 and 19 % of N_2 will be produced. As Figure 6(a) displays, at 3 minutes, the NH_3, H_2, N_2, and NO concentrations were approximately 0.6 %, 5.0 %, 15.6 %, and 431 ppm, respectively. Based on the iron ore weight loss rate, it can be inferred that the reaction is theoretically in the stage of Fe_2O_3 to Fe_3O_4 at the conditions of 2 minutes. In this case, the H_2 to N_2 ratio at the reactor outlet was less than 1, indicating that a large amount of H_2 generated from NH_3 decomposition participates in the L1 reduction reaction. H_2 predominantly drives the reduction process of lump ores, which is consistent with previous research [27]. Related studies also indicated that the NH_3 metallurgical process involves not only the indirect reduction of H_2 produced by NH_3 decomposition [37], but also the direct reduction of NH_3, although the proportion of NH_3 direct reduction is relatively small. In addition, the formation of NO revealed that NH_3 takes part in the early-stage reduction of iron ore. The highest concentration of NO was observed at 3 minutes. As the reduction progressed, the concentration of NO gradually decreased, which was due to the gradual decrease in O content in the ores. When the concentration of NH_3 was constant, increasing the temperature would promote the reduction reaction. Therefore, at a reaction time of 180 minutes, the concentration of NO at the outlet of the reactor gradually decreased. The NO concentration at the outlet was between (0–12) ppm, indicating that ultra-low NO emissions can be achieved during the NH_3-based metallurgy process when Fe was produced. Moreover, the rate of H_2 generation was relatively fast at the beginning of the reaction and gradually decreased as the reaction progressed. H_2 and NH_3 concentrations stabilized at about 51 % and 1 %, respectively, demonstrating that iron-catalyzed NH_3 decomposition takes precedence in the final stages of the reaction.

https://doi.org/10.64486/m.65.3.9

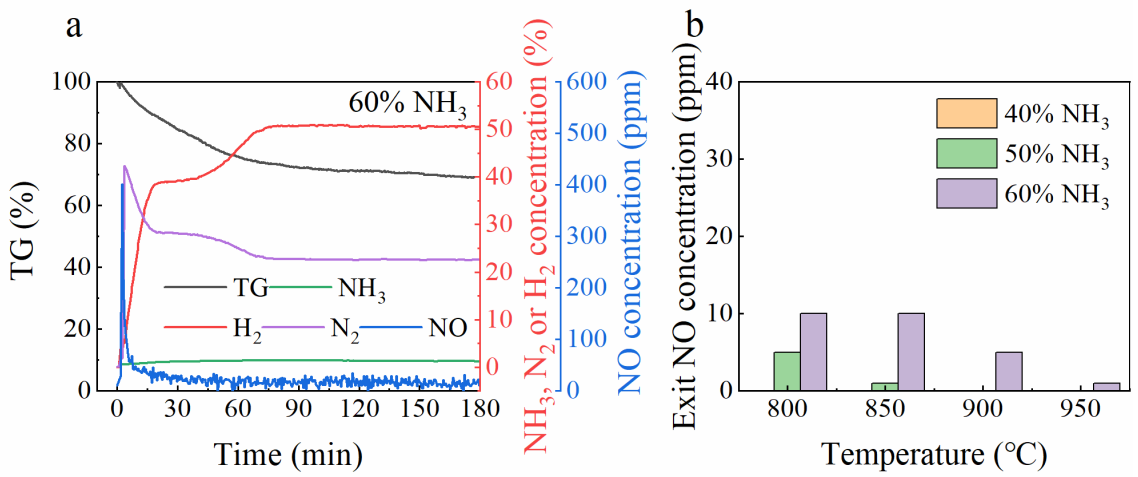

Figure 6. (a) TG curves and outlet gas concentrations change during the reduction of L1 by 60 % NH_3 at 900 °C. (b) Variation in NO concentration at the outlet during the reduction of L1 at 180 minutes with different concentrations of NH_3 within the temperature range of 800 °C–950 °C.

3.2. Reduction Disintegration Behavior

The low-temperature reduction disintegration behavior of L1 by different concentrations of NH_3 at 500 °C was investigated. Figures 7(a) and 7(b) display the XRD patterns, α, and RDI of samples reduced by NH_3 at different concentrations. As Figure 7(a) indicates, the original goethite completely decomposed, and hematite became the main phase. Alongside Fe_2O_3, the sample also exhibited peaks corresponding to Fe_3O_4 (JCPDS 11-0614) [41] at 2θ = 18.3°, 30.1°, 37.1°, 43.1°, 57.0°, and 74.1° in the samples of L1-500 °C-20 % NH_3, L1-500 °C-40 % NH_3, and L1-500 °C-60% NH_3. The intensity of Fe_2O_3's diffraction peaks declined as the NH_3 concentration increased. Meanwhile, the α value increased with the increase of NH_3 concentration (as shown in Figure 7(b)), indicating that the reduction of $Fe_2O_3 \rightarrow Fe_3O_4$ is promoted. Under the experimental conditions, the $RDI_{+6.3\,mm}$ of L1 was greater than 89 % at three NH_3 concentration conditions. Moreover, the $RDI_{+3.15\,mm}$ value declined as the NH_3 concentration increased. Increasing the concentration of NH_3 will intensify the low-temperature reduction disintegration degree of lump ores. Notably, NH_3 decomposition exhibits a low rate at 500 °C [42], so it can be inferred that H_2 has a relatively small impact on the reduction disintegration degree of lump ores.

Figures 7(c) and 7(d) reveal the adsorption-desorption curves of the sample after reduction with different concentrations of NH_3. According to the IUPAC classification, the adsorption-desorption curves of L1 and the reduced samples both exhibited type IV isotherms [43]. The adsorption-desorption curves of the reduced sample were accompanied by a significant H3 hysteresis loop, indicating the presence of mesopores in the sample and an irregular pore structure. The peak in the pore size distribution curve of the sample after NH_3 reduction showed a rightward shift trend, reflecting an expansion in the sample's pore size (in Figure 7(d)). Table 4 lists the specific surface area and pore structure information of samples after the reduction of L1 with different concentrations of NH_3 at 500 °C. The larger specific surface area of L1 provides favorable conditions for NH_3 diffusion into the interior of L1. The NH_3-reduced samples exhibited greater specific surface area, total pore volume, and average pore diameter compared to the original ore. Based on the XRD results analysis, this phenomenon can be attributed to the conversion of hematite (hexahedral crystal system) to magnetite (cubic crystal system) [44] under these conditions, resulting in lattice distortion and the formation of larger pore structures. Meanwhile, significant internal stress was generated during the reduction process, leading to fragmentation and disintegration of the lump ores.

https://doi.org/10.64486/m.65.3.9

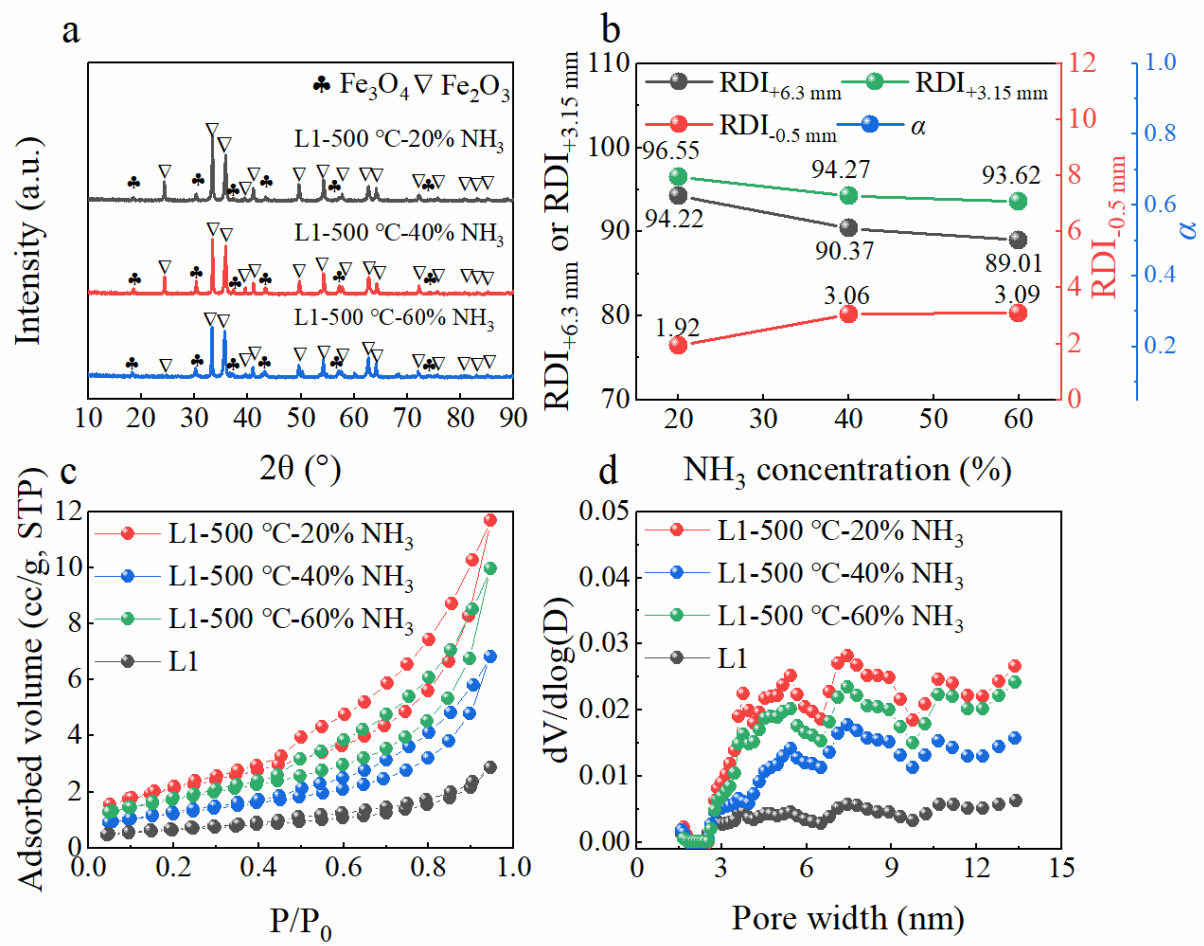

Figure 7. (a) XRD pattern, (b) the value of RDI and α, (c) adsorption-desorption curves and (d) pore size distribution of the samples.

Table 4. Specific surface area and pore structure information of samples before and after reduction with different concentrations of NH_3.

Reduced sample	Specific surface area m^2/g	Total pore volume cm^3/g	Average pore diameter nm
L1	2.32	4.42E-03	7.63
L1-500 °C-20 % NH_3	7.61	1.81E-02	9.50
L1-500 °C-40 % NH_3	4.44	1.06E-02	9.53
L1-500 °C-60 % NH_3	6.24	1.54E-02	9.89

Figure 8 shows the SEM-EDS analysis of the samples of L1-500 °C-20 % NH3 and L1-500 °C-60 % NH3. After heating, most of the dark gray goethite in the raw ore decomposed, resulting in higher porosity in the reduced sample compared to the original ores [21]. The surface scan results showed that the distribution of Fe and O elements is extremely uniform. The ratio of Fe to O in the regions of points 1 and 2 was close to 1, indicating that the regions of points 1 and 2 correspond to FeO. The content of Fe was higher in point 3, while the content of O was lower. The ratio of Fe to O in the area of point 4 was close to 0.67, indicating that this organization may correspond to hematite. The content of Fe in the area of point 5 was

https://doi.org/10.64486/m.65.3.9

higher than that of O, indicating that the light gray area may correspond to a mixture of Fe3O4 and Fe2O3. Point 6 may correspond to impurities in the gangue.

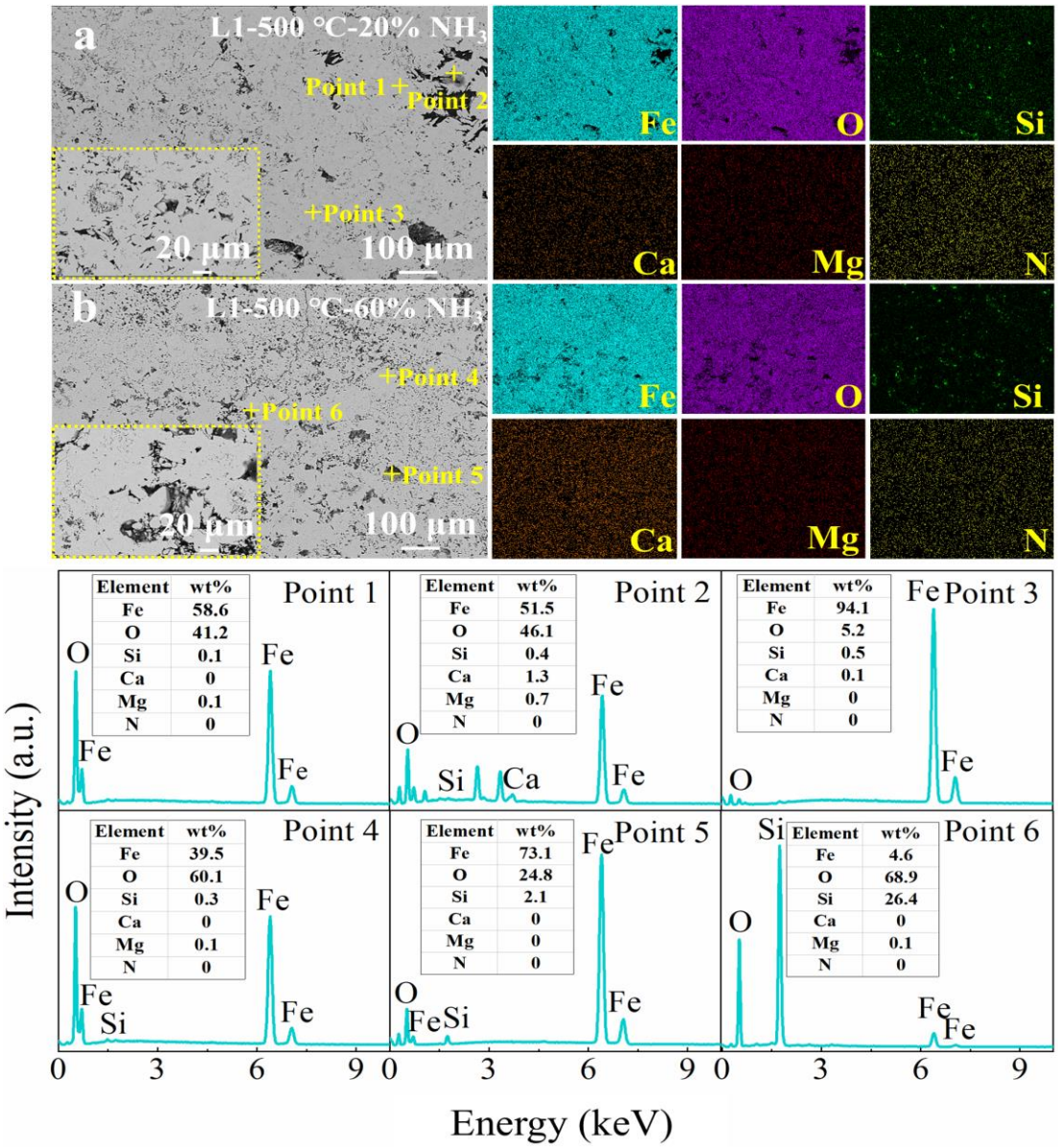

Figure 8. SEM-EDS analysis of the reduced samples: (a) L1-500 ℃-20 % NH_3, and (b) L1-500 ℃-60 % NH_3.

The OM images before and after the reduction of L1 by different NH_3 concentrations are illustrated in Figure 9. Compared with Figure 5, the sample reduced at 500 ℃ still exhibits the morphology of magnetite filling between hematite. Compared with the original ore, the reduced sample showed more pores, which was consistent with Figure 8 and the analysis of specific surface area.

https://doi.org/10.64486/m.65.3.9

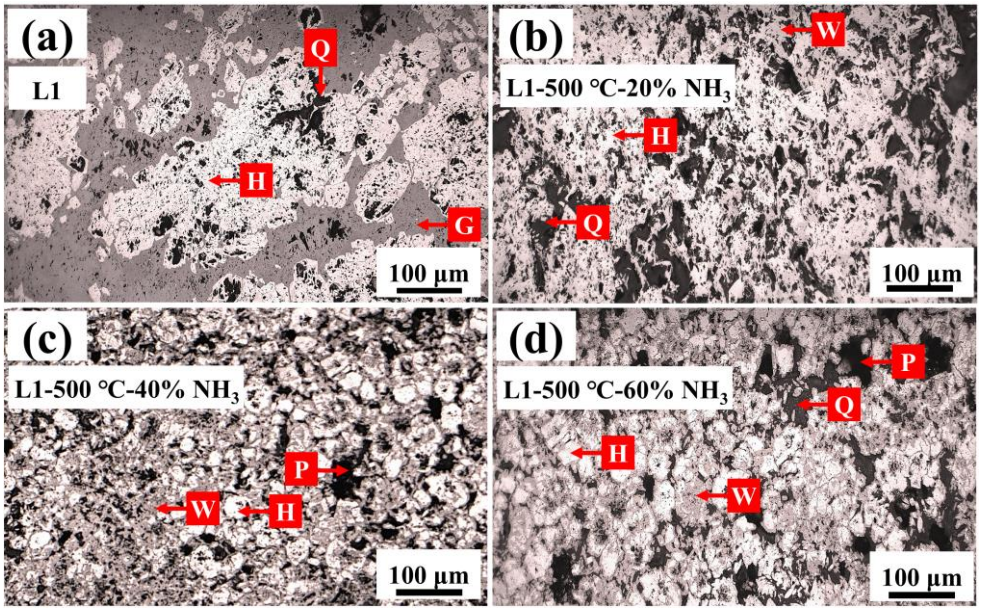

Figure 9. OM images of the cross-section of the samples: (a) L1, (b) L1-500 °C-20 % NH_3, (c) L1-500 °C-40 % NH_3, and (d) L1-500 °C-60 % NH_3. (P: pore. Q: quartz. H: hematite. G: goethite. W: wüstite.)

3.3. Reduction Kinetics

Studying the kinetics of gas-solid reactions plays a guiding role in the production of NH_3-based metallurgy processes. According to Figure 3, the α value undergoes multiple changes over time. Therefore, the reduction process of L1 was considered to improve the accuracy of calculations. Using model-fitting and model-free methods, the kinetics of 60 % NH_3 reduction of L1 ore was investigated, ranging from 800 °C to 950 °C.

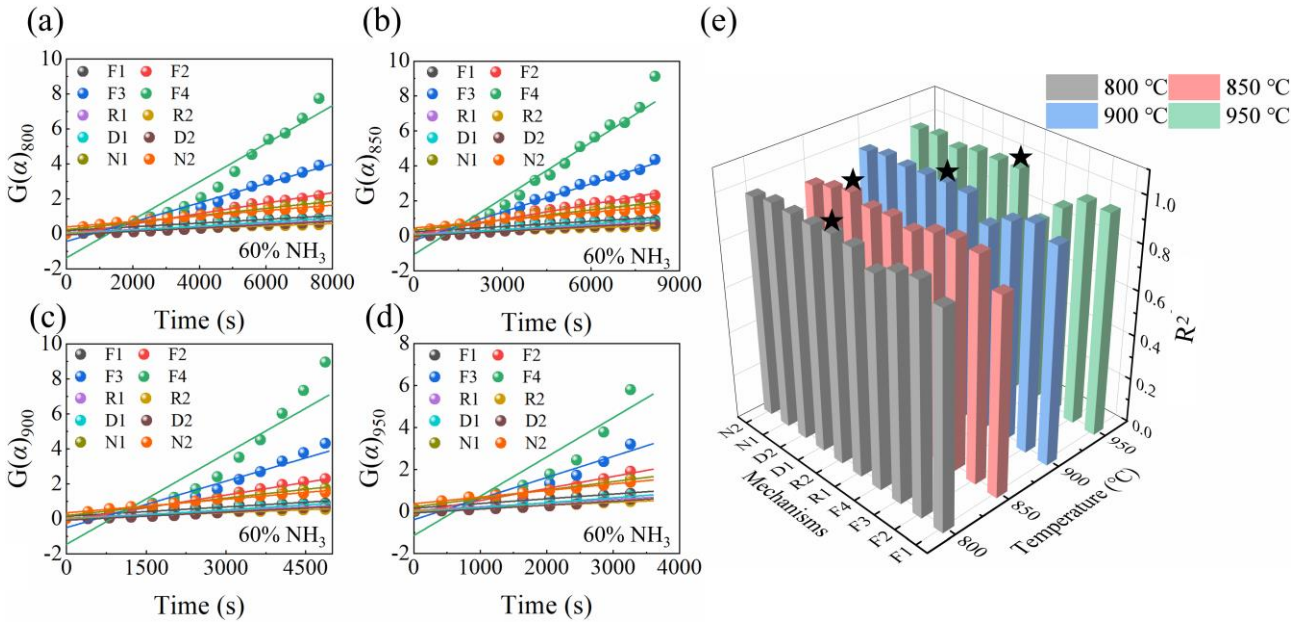

Figure 10. Results of linear fitting between G(α) and t during 60 % NH_3 reducing L1 by the model-fitting method at different reduction temperatures: (a) 800 °C, (b) 850 °C, (c) 900 °C, and (d) 950 °C. (e) The R^2 value of the fitted lines in Figure 10(a), Figure 10(b), and Figure 10(c), and Figure 10(d). (★ denotes the mechanism with the highest R^2)

https://doi.org/10.64486/m.65.3.9

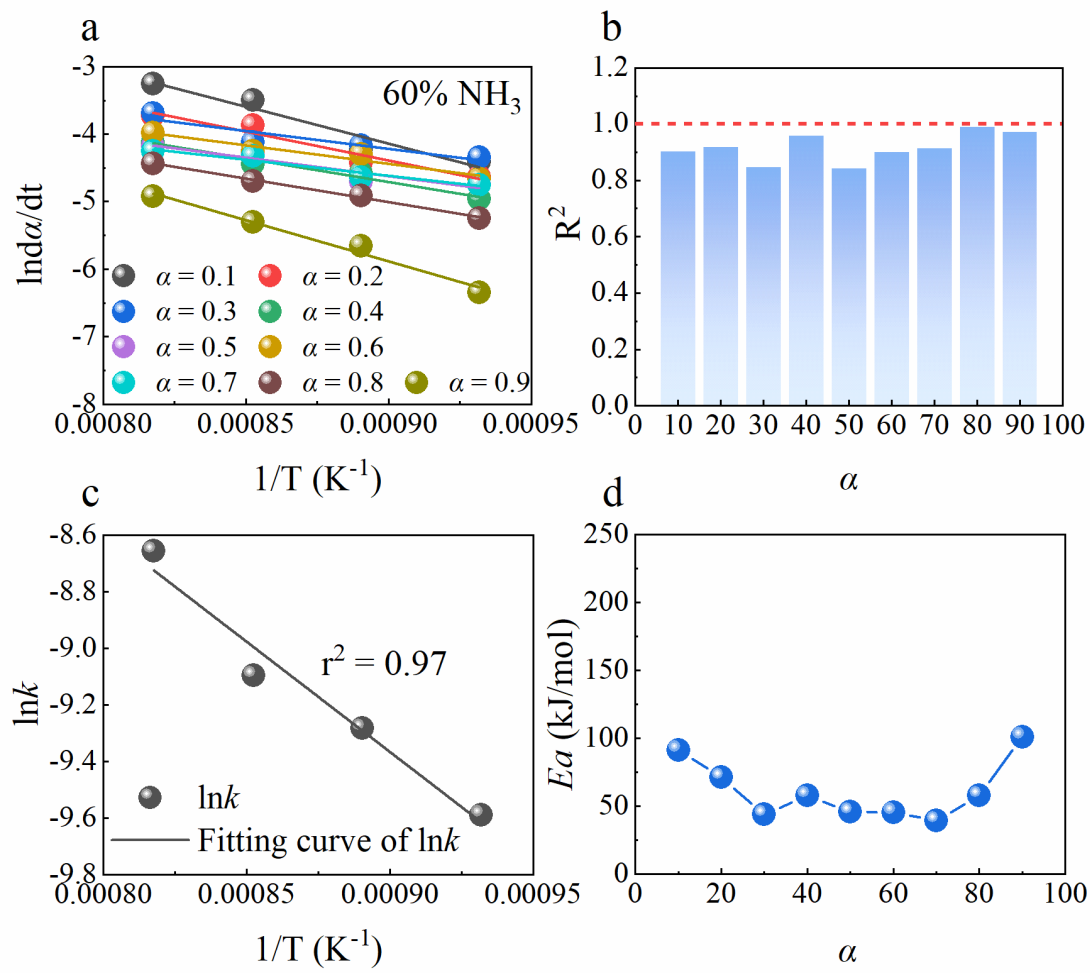

Figure 11. (a) Results of linear fitting between ln (dα/dt) and 1/T during the reduction of L1 by 60 % NH_3, as well as (b) the R^2 value for the fitting lines in Figure 11(a). (c) Results of linear fitting between lnk and t during the reduction of L1 by 60 % NH_3 in the range of 800 °C–950 °C by the model-fitting method. (d) The apparent Ea during the reduction of L1 by 60 % NH_3 varies with α by the model-free method.

The results above clearly show that the R^2 values exceed 0.97, demonstrating an excellent fit. The slope of the best-fit line corresponds to the k at different temperatures, as shown in Table 5.

Table 5. Reduction kinetics parameters of L1 reduction by 60 % NH_3 in the range of 850 °C–950 °C.

T/°C	k/s^{-1}	Mechanism	Ea/kJ/mol	A/s^{-1}	Average Ea/kJ/mol
950	1.74E-04	Contracting sphere	64.78	0.09	61.60
900	1.12E-04				
850	9.30E-05	diffusion			
800	6.85E-05	Contracting sphere			

To improve the accuracy of the calculation, a model-free approach was employed to analyze the kinetics of the 60 % NH_3 reduction of L1. As shown in Figure 11(a), the varying slopes of the fitted lines for lndα/dt versus 1/T suggest differences in the apparent Ea of the reduction. Meanwhile, the range of R^2 values for the fitting line was between 0.843–0.992 (in Figure 11(b)). As Figure 11(c) indicates, the fitted line achieves an R^2 of 0.97. According to equation (6), the values of Ea and A were 64.78 kJ/mol and 0.09 s^{-1}, respectively. As Table 5

https://doi.org/10.64486/m.65.3.9

summarizes, results from the model-free approach revealed that the apparent Ea is between 39.36 kJ/mol and 101.23 kJ/mol. Under the condition of $\alpha = 0.9$, the apparent Ea reached its peak. The reduction reaction of lump ore conforms to the unreacted nucleus theory, which means that the newly formed Fe covers the sample surface during later stages, increasing resistance to reducing gas diffusion into the interior [45]. In addition, the average apparent Ea calculated by the model-free method was 61.60 kJ/mol, closely matching the Ea calculated by the model-fitting approach, reflecting the accuracy of the kinetic calculation.

4. Conclusions

In this paper, the effect of gas concentration on the reduction and disintegration behaviors of NH_3 reduction lump ores was examined. The reduction kinetics of lump ores using 60 % NH3 were investigated. The primary results are summarized below:

1. Using 60 % NH_3, the metallization rate of the product varied between 94.58 % and 98.94 % across temperatures of 800 °C to 950 °C. At 800 ℃ and 850 ℃, the reduced sample contained approximately 10 %–12 % SiO_2 and 4 %–6 % FeO. As the temperature increased, good interconnection between iron phases in the reduced sample was observed. The change in gas concentration indicates that H_2 produced by NH_3 decomposition in the early stage of the reaction participates in the reaction and dominates the reduction process. Moreover, the concentration of NO can reach up to 431 ppm, indicating a low reduction role of NH_3. As the ore's oxygen content declined, the NO concentration also dropped to (0–12) ppm.

2. Under the conditions of NH3 concentrations of 20 %, 40 %, and 60 %, the RDI+3.15 mm was 94.22 %, 90.37 %, and 89.01 %, respectively. Raising the NH3 concentration enhances the reduction process from Fe2O3→Fe3O4, thereby improving the reduction disintegration degree of the lump ores. The specific surface area and average pore size of the samples increased after reduction.

3. The reduction of lump ores aligns with the diffusion and geometrical contraction models. Using the model-fitting method, the activation energy was calculated as 64.78 kJ/mol at a 60 % NH3 concentration. The model-free method results showed an average apparent Ea of 61.60 kJ/mol for α values ranging from 0.1 to 0.9.

Ammonia metallurgy is still in its infancy, and there are currently no international standards to investigate the metallurgical properties of iron ore under NH3 conditions. This study only conducted a preliminary evaluation of the reduction degree, reduction pulverization index, and kinetics of ammonia reduction of lump ores. Further research on the reaction mechanism is needed in the future.

Acknowledgments: The authors highly appreciate the Hebei Province Major Science and Technology Support Program Project (24294001Z) and the National Key R&D Program of China (No. 2022YFE0208100) for their financial support. The authors also acknowledge the Fundamental Research Funds for Liaoning Universities (LJ222410146023). In addition, the author would like to thank Hegang Group for their assistance and financial support in the experiment.

References

[1] W. Liang, "Life cycle assessment of blast furnace ironmaking processes: A comparison of fossil fuels and biomass hydrochar applications," Fuel, vol. 345, pp. 128138, 2023, https://doi.org/10.1016/j.fuel.2023.128138.

[2] K. Ma, "Utilization and impacts of hydrogen in the ironmaking processes: A review from lab-scale basics to industrial practices," Int. J. Hydrogen Energy, vol. 46, no. 52, pp. 26646-26664, 2021, https://doi.org/10.1016/j.ijhydene.2021.05.095.

[3] A. Devlin, "Global green hydrogen-based steel opportunities surrounding high quality renewable energy and iron ore deposits," Nat. Commun., vol. 14, no. 1, pp. 2578, 2023, https://doi.org/10.1038/s41467-023-38123-2.

[4] A. Heikkilä, "Reduction of Iron Ore Pellets, Sinter and Lump Ore under Simulated Blast Furnace Conditions," Steel Res. Int., vol. 91, 2020, https://10.1002/srin.202000047.

https://doi.org/10.64486/m.65.3.9

[5] D. Zhu, "Study of Mineralogy and Metallurgical Properties of Lump Ores," Metals, vol. 12, no. 11, pp. 1805, 2022, https://doi.org/10.3390/met12111805.

[6] J. Zhang, "The Temperature of Pretreatment on Microstructure Change of Lump Ore and Improvement of Metallurgical Properties," Steel Res. Int., vol. 95, no. 8, pp. 2400074, 2024, https://doi.org/10.1002/srin.202400074.

[7] X. Ma, "Experimental Research on the Metallurgical Properties and Cokes' Solution-Loss Reaction of Lump Ores in the H_2O-CO_2 Atmosphere in the Hydrogen-Rich Blast Furnace," Metall. Mater. Trans. B, vol. 55, no. 5, pp. 3879-3893, 2024, https://10.1007/s11663-024-03216-w.

[8] H. Liu, "An overview of the role of goethite surfaces in the environment," Chemosphere, vol. 103, pp. 1-11, 2014, https://doi.org/10.1016/j.chemosphere.2013.11.065.

[9] S. Wu, "Reduction Disintegration Behavior of Lump Ore in COREX Shaft Furnace," ISIJ Int., vol. 55, no. 8, pp. 1608-1616, 2015, https://10.2355/isijinternational.ISIJINT-2014-417.

[10] T. Murakami, "Reduction Disintegration Behavior of Iron Ore Sinter under High H_2 and H_2O Conditions," ISIJ Int., vol. 52, pp. 1447-1453, 2012, https://doi.org/10.2355/isijinternational.52.1447.

[11] Z. Zhao, "Reduction Behavior of Lump Ore and Its Applicability During Hydrogen-Based Shaft Furnace Process," J. Sustain. Metall., vol. 10, pp. 2534-2544, 2024, https://10.1007/s40831-024-00925-z.

[12] V. Strezov, "Structural deterioration of iron ore particles during thermal processing," Int. J. Miner. Process., vol. 100, no. 1, pp. 27-32, 2011, https://doi.org/10.1016/j.minpro.2011.04.005.

[13] L. Niu, "Lump Iron Ore Pre-heating Treatment to Improve Softening-Melting Performance and Reduce Energy Consumption in Ironmaking Process," JOM, vol. 74, no. 7, pp. 2733-2741, 2022, https://10.1007/s11837-022-05301-4.

[14] M. Mizutani, "Influence of Reducing Gas Composition on Disintegration Behavior of Iron Ore Agglomerates," ISIJ Int., vol. 57, pp. 1499-1508, 2017, https://10.2355/isijinternational.ISIJINT-2017-074.

[15] C. Scharm, "Direct reduction of iron ore pellets by H_2 and CO: In-situ investigation of the structural transformation and reduction progression caused by atmosphere and temperature," Miner. Eng., vol. 180, pp. 107459, 2022, https://doi.org/10.1016/j.mineng.2022.107459.

[16] H. Guo and X.-M. Guo, "Mechanism of Low-Temperature Reduction Degradation of Alumina-Containing Hematite Solid Solution Below 550 °C," Metall. Mater. Trans. B, vol. 49, no. 6, pp. 3513-3521, 2018, https://10.1007/s11663-018-1426-1.

[17] T. Murakami, "Effect of the Reduction of Calcium Ferrite on Disintegration Behavior of Sinter under High Hydrogen Atmosphere," ISIJ Int., vol. 55, pp. 1197-1205, 2015, https://10.2355/isijinternational.55.1197.

[18] T. Murakami, "Reduction and Disintegration Behavior of Sinter under N_2–CO–CO_2–H_2–H_2O Gas at 773 K," ISIJ Int., vol. 55, pp. 1181-1187, 2015, https://10.2355/isijinternational.55.1181.

[19] Z. Abdin, "A review of renewable hydrogen hybrid energy systems towards a sustainable energy value chain," Sustain. Energ. Fuels, vol. 7, no. 9, pp. 2042-2062, 2023, https://doi.org/10.1039/D3SE00099K.

[20] Q. Hao, "The flammability limits and explosion behaviours of hydrogen-enriched methane-air mixtures," Experimental Thermal and Fluid Science, vol. 126, no. 4, pp. 110395, 2021, https://10.1016/j.expthermflusci.2021.110395.

[21] H. Liu, "Thermal treatment of natural goethite: Thermal transformation and physical properties," Thermochim. Acta, vol. 568, pp. 115-121, 2013, https://doi.org/10.1016/j.tca.2013.06.027.

[22] A. Klerke, "Ammonia for hydrogen storage: Challenges and opportunities," J. Mater. Chem., vol. 18, pp. 2304-2310, 2008, https://doi.org/10.1039/B720020J.

[23] M. Aziz, "Ammonia as Effective Hydrogen Storage: A Review on Production, Storage and Utilization," Energies, vol. 13, no. 12, pp. 3062, 2020, https://doi.org/10.3390/en13123062.

[24] R. Lan, "Ammonia and related chemicals as potential indirect hydrogen storage materials," Fuel and Energy Abstracts, vol. 37, 2012, https://doi.org/10.1016/j.ijhydene.2011.10.004.

[25] N. Yasuda, "Reduction and Nitriding Behavior of Hematite with Ammonia," ISIJ Int., vol. 55, no. 4, pp. 736-741, 2015, https://doi.org/10.2355/isijinternational.55.736.

[26] Y. Ma, "Reducing Iron Oxide with Ammonia: A Sustainable Path to Green Steel," Adv. Sci., vol. 10, no. 2300111, pp. 1-7, 2023, https://doi.org/10.1002/advs.202300111.

[27] S. Hosokai, "Ironmaking with Ammonia at Low Temperature," Environ. Sci. Technol., vol. 45, pp. 821-826, 2011, https://doi.org/10.1021/es102910q.

[28] I. Iwamoto, "Reduction Behaviors and Generated Phases of Iron Ores using Ammonia as Reducing Agent," ISIJ Int., vol. 62, no. 12, pp. 2483-2490, 2022, https://doi.org/10.2355/isijinternational.ISIJINT-2022-155.

[29] N. Tsubouchi, "High Catalytic Performance of Fine Particles of Metallic Iron Formed from Limonite in the Decomposition of a Low Concentration of Ammonia," Catal. Lett., vol. 105, no. 3, pp. 203-208, 2005, https://doi.org/10.1007/s10562-005-8691-8.

[30] N. Tsubouchi, "Catalytic Performance of Limonite in the Decomposition of Ammonia in the Coexistence of Typical Fuel Gas Components Produced in an Air-Blown Coal Gasification Process," Energ Fuel, vol. 21, no. 6, pp. 3063-3069, 2007, https://10.1021/ef070096j.

[31] Y. Liu, "Study on the reaction characteristics and kinetics of reducing iron ore pellet by utilization of ammonia," Energy Conversion and Management, vol. 343, pp. 120235, 2025, https://doi.org/10.1016/j.enconman.2025.120235.

[32] M. Tadic, "Hydrothermal synthesis of hematite (α-Fe_2O_3) nanoparticle forms: Synthesis conditions, structure, particle shape analysis, cytotoxicity and magnetic properties," J. Alloys Compd., vol. 792, pp. 599-609, 2019, https://doi.org/10.1016/j.jallcom.2019.03.414.

[33] A. Malathi, "Rod-on-flake α-FeOOH/BiOI nanocomposite: Facile synthesis, characterization and enhanced photocatalytic performance," Colloids Surf., A, vol. 537, pp. 435-445, 2018, https://doi.org/10.1016/j.colsurfa.2017.10.036.

[34] P.Y. Jia, "Luminescence properties of sol-gel derived spherical SiO_2@$Gd_2(WO_4)_3$:Eu^{3+} particles with core-shell structure," Chem. Phys. Lett., vol. 424, no. 4, pp. 358-363, 2006, https://doi.org/10.1016/j.cplett.2006.04.088.

[35] A. Khawam and D.R. Flanagan, "Solid-State Kinetic Models: Basics and Mathematical Fundamentals," J. Phys. Chem. B, vol. 110, no. 35, pp. 17315-17328, 2006, https://doi.org/10.1021/jp062746a.

[36] F. He, "Gas-based reduction and nitridation for synthesis of vanadium nitride: Kinetics and mechanism," Powder Technol., vol. 427, pp. 118757, 2023, https://doi.org/10.1016/j.powtec.2023.118757.

[37] T. Triana, "Iron Oxide Direct Reduction and Iron Nitride Formation Using Ammonia: Review and Thermodynamic Analysis," J. Sustain. Metall., vol. 10, no. 3, pp. 1428-1445, 2024, https://doi.org/10.1007/s40831-024-00860-z.

[38] J. Zhao, "FeO–CeO_2 nanocomposites: an efficient and highly selective catalyst system for photothermal CO_2 reduction to CO," NPG Asia Mater., vol. 12, no. 1, pp. 1-5, 2020, https://doi.org/10.1038/s41427-019-0171-5.

[39] Y. Liu, "Direct reduction of ferric oxide by ammonia and hydrogen in gas-based ironmaking process: Reaction characteristics, kinetics, and adsorption behaviors," Int. J. Hydrogen Energy, vol. 105, pp. 1057-1068, 2025, https://doi.org/10.1016/j.ijhydene.2025.01.371.

[40] K.A. Farley, "Dehydration of goethite during vacuum step-heating and implications for he retentivity characterization," Chem. Geol., vol. 663, pp. 122254, 2024, https://doi.org/10.1016/j.chemgeo.2024.122254.

[41] C.-C. Lin and J.-M. Ho, "Structural analysis and catalytic activity of Fe_3O_4 nanoparticles prepared by a facile co-precipitation method in a rotating packed bed," Ceram. Int., vol. 40, no. 7, Part B, pp. 10275-10282, 2014, https://doi.org/10.1016/j.ceramint.2014.02.119.

[42] S. Mukherjee, "Low-temperature ammonia decomposition catalysts for hydrogen generation," Applied Catalysis B: Environmental, vol. 226, pp. 162-181, 2018, https://doi.org/10.1016/j.apcatb.2017.12.039.

[43] M.A. Al-Ghouti and D.A. Da'ana, "Guidelines for the use and interpretation of adsorption isotherm models: A review," J. Hazard. Mater., vol. 393, pp. 122383, 2020, https://doi.org/10.1016/j.jhazmat.2020.122383.

[44] J.-f. Lu and C.-J. Tsai, "Hydrothermal phase transformation of hematite to magnetite," Nanoscale Research Letters, vol. 9, no. 1, pp. 230, 2014, https://10.1186/1556-276X-9-230.

[45] E.-H. Kwon, "Modified Unreacted Core Model for Reduction of Manganese Ore by CO Gas," Metals and Materials International, vol. 28, no. 6, pp. 1517-1524, 2022, https://10.1007/s12540-021-01020-8.

https://doi.org/10.64486/m.65.3.9